SAND2019-0516C
2019-01-0553

Dilution and injection pressure effects on ignition and onset of soot at threshold-sooting conditions by simultaneous PAH-PLIF and soot-PLII imaging in a heavy duty optical diesel engine

Author, co-author (Do NOT enter this information. It will be pulled from participant tab in MyTechZone)
Affiliation (Do NOT enter this information. It will be pulled from participant tab in MyTechZone)

Abstract

Although accumulated in-cylinder soot can be measured by various optical techniques, discerning soot formation rates from oxidation rates is more difficult. Various optical measurements have pointed toward ways to affect in-cylinder soot oxidation, but evidence of effects of operational variables on soot formation is less plentiful. The formation of soot and its precursors, including polycyclic aromatic hydrocarbons (PAHs), are strongly dependent on temperature, so factors affecting soot formation may be more evident at low-temperature combustion conditions. Here, in-cylinder PAHs are imaged by planar laser-induced fluorescence (PAH-PLIF) using three different excitation wavelengths of 355, 532, and 633 nm, to probe three different size-classes of PAH from 2-3 to 10+ rings. Simultaneous planar laser-induced incandescence of soot (soot-PLII) using 1064-nm excitation provides complementary imaging of soot formation near inception. To achieve low combustion temperatures at the threshold of PAH and soot formation, the engine operating conditions are highly diluted, with intake-O_2 mole-fractions as low as 7.5%. The optical diagnostics show that increasing dilution delays the inception of PAH by over 2.5 ms as the intake-O_2 mole-fraction decreases from 15.0% to 9.0%. At 7.5% intake-O_2, no large PAH or soot are formed, while the 9.0% intake-O_2 condition forms PAH but virtually no detectable soot. Conditions with 10.0% or more intake-O_2 form both PAH and soot. For the threshold-sooting condition with 10.0% intake-O_2, large PAH typically forms broadly throughout the cross-section of the downstream jets and along the bowl-wall. Soot appears after PAH, and in narrower ribbons in the jet-jet interaction region. These soot ribbons are on the periphery of the PAH, near the diffusion flame, where the highest temperatures are expected. With increasing intake-O_2, the delay time between soot and PAH shortens, and soot tends to shift upstream to the jet region prior to wall impingement, though still on the periphery of the PAH. The spatial distributions of PAH and soot overlap slightly under these threshold-sooting conditions, with soot typically surrounding the PAH. This may indicate that temperatures are only high enough for soot formation on the jet periphery, near the diffusion flame. The minimal overlap also suggests that PAHs are rapidly consumed and/or adsorbed when soot is formed. Additionally, increasing the fuel-injection pressure from 533 to 800 and then to 1200 bar increases soot and large PAH formation, which is opposite to the trend for conventional diesel combustion.

Introduction

Soot and nitrogen oxides (NO_x) are two pollutant emissions of concern from internal combustion engines [1]. The soot-NO_x trade-off is the classic challenge of diesel engines, and can be affected by exhaust-gas recirculation (EGR). Currently, most engine manufactures use moderate EGR to reduce engine-out NO_x to a level where emissions-controls can mitigate soot and NO_x emissions to comply with regulatory limits. Low-temperature combustion (LTC) using EGR has been shown to reduce both soot and NO_x to levels at which little or even no emissions-controls are required for soot and/or for NO_x, and sometimes, to also achieve higher efficiency [2]. Dempsey et al. [3], among others, have described how LTC avoids soot and NO_x formation regions in the in-cylinder operating space of equivalence ratio (ϕ) and temperature: LTC mixtures that are rich enough to form soot do not achieve sufficiently high temperatures for soot formation, and leaner LTC regions are likewise too cold for excessive NO_x formation. Even so, scientific understanding of many aspects of diesel soot and/or polycyclic aromatic hydrocarbons (PAHs) formation is still incomplete.

PAHs are produced by incomplete combustion of hydrocarbon fuels [4] and are known to be soot precursors [5]. Many PAHs are also toxic pollutants [6]. Though LTC has the potential of avoiding both NO_x and soot, the in-cylinder processes by which LTC can potentially reduce PAH formation, and how in-cylinder processes might be utilized to reduce soot at less extreme LTC conditions, is still not clear. To understand how in-cylinder processes of LTC may be manipulated to minimize soot formation, it is essential to understand the interaction and transition between PAH and soot.

Various methods can measure in-cylinder PAH and soot, and many useful techniques employ laser diagnostics. Laser diagnostics to probe both PAH and soot together in engines were demonstrated in the late 1990s [7-9]. PAH-planar laser-induced fluorescence (PAH-PLIF) has been combined with soot-planar laser-induced incandescence (soot-PLII) to visualize PAH- and soot-formation processes. Other optical experimental and numerical studies on PAH and soot were reported by researchers using gaseous fuels [10-12].

While laser diagnostics can provide non-intrusive and useful information, they can be limited to some degree by various interferences, especially when using ultraviolet (UV) lasers. One

source of interference can be due to fuel components. Commercial diesel fuel is a complex mixture of thousands of components, many of which fluoresce at wavelengths that interfere with the desired fluorescence of species like PAH. Therefore, PAH-PLIF experiments typically utilize surrogate diesel fuels that yield low fluorescence interference [13-16]. For example, Lermaire et al. [15] used a surrogate of 80% n-decane and 20% α-methylnaphthalene. They reported that the PAH and soot are quite spatially similar (in shape and intensity) in both a diesel engine and in a piloted jet burner. Zhou et al. [16] performed PAH-PLIF and soot-PLII in a laminar flame at elevated pressures up to 3.0 bar with n-heptane fuel. By comparing the PAH-PLIF and soot-PLII signal distribution, they concluded that PAHs were mostly surrounded by soot and in the lower part of the flame (upstream).

Simultaneous PAH-PLIF and soot-PLII have also been demonstrated using diesel surrogate fuels in the optical engine of this study [17-19]. Most recently, Leermakers et al. [17] imaged PAH-PLIF using three discrete excitation wavelengths (266, 532, and 633 nm) to reveal the spatial and temporal growth of PAH molecules. As PAHs grow and accumulate more carbon/aromatic rings, their spectral absorption range shifts to longer wavelengths [17]. Thus, three laser wavelengths are used for PAH-PLIF excitation to probe the growth of PAH. Prior to that, PAH-PLIF was excited at 532 nm only, which showed that the time from PAH appearance to soot formation is delayed by increasing dilution [18]. In another study using a 355-nm laser for formaldehyde-PLIF, spectral analysis of the fluorescence emissions showed that both formaldehyde and PAH signatures, and that the signal from the two species was separated both temporally and spatially [19].

This paper builds on previous work by focusing on soot and PAH formation. While previous works in this facility and in the literature have provided useful information on the spatial and temporal evolution of PAH and total soot at LTC conditions [20], the data to date provide insufficient distinction between formation and oxidation effects on soot. While total soot and PAH are readily measured, distinguishing soot formation effects from soot oxidation effects is difficult. Here, we aim to build understanding of soot formation processes by probing PAH and soot at threshold-sooting conditions with low intake-O_2 mole fractions. At high levels of dilution, and near inception, accumulation of PAH and soot is expected to be dominated by formation processes, with minimal contributions from oxidation. Hence, changes in the PAH and/or soot distributions with various parameter variations should provide insight into the formation part of the accumulated in-cylinder PAH and soot.

The experimental setup and engine operating conditions are described first. Thereafter, the results from optical engine data are presented and discussed in subsections: Effects of Dilution on Large PAH and Soot, Effects of CR Fuel-Pressure on Large PAH and Soot, and Distribution of Dilution on Small and Medium PAHs. Finally, the conclusions are summarized.

Experimental Setup

Engine Setup

The experiments use the Sandia/Cummins single-cylinder heavy-duty optical engine, which is based on the Cummins N-series production engine and is modified for optical access. Figure 1 shows a side-view schematic of the engine and optics setup, and Table 1 summarizes the specifications of the engine, injector and fuel.

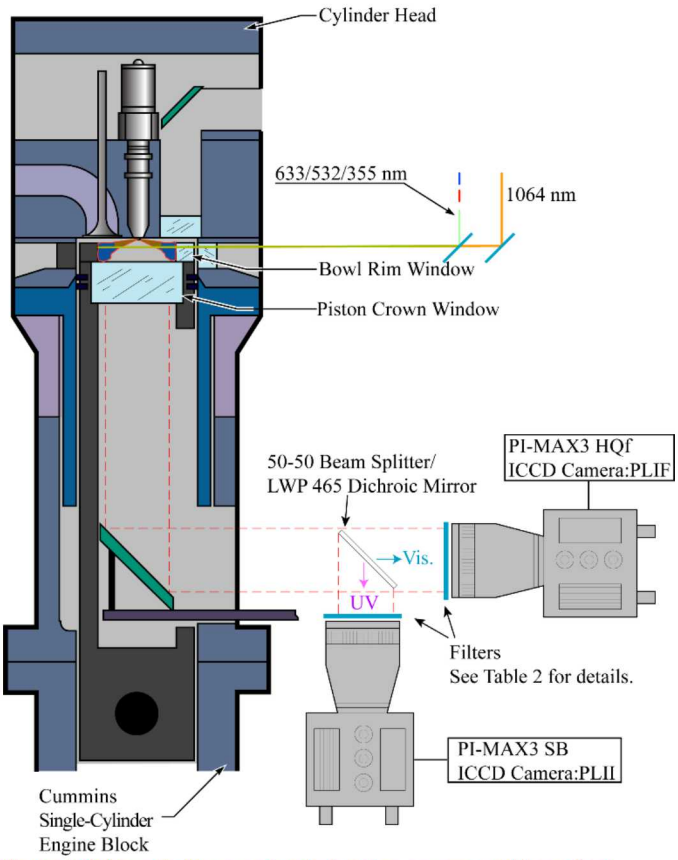

Figure 1: Schematic diagram of optical engine, cameras and laser-sheet alignment.

Table 1: Engine, injector, and fuel specifications

Engine base type	Cummins N-14, DI diesel
Number of cylinders	1
Number of intake valves	2
Number of exhaust valves	1*
Combustion chamber	Quiescent, direct injection
Swirl ratio	0.5
Bore × stroke, [cm]	13.97 × 15.24
Bowl width, depth, [cm]	9.78, 1.55
Displacement, [liters]	2.34
Connecting rod length, [cm]	30.48
Geometric compression ratio	11.2:1
Fuel injector type	Common-rail, solenoid actuated Delphi DFI-1.5
Number of holes & arrangement	8, equally-spaced
Nominal orifice diameter, [mm]	0.131
Included spray angle	156°
Fuel type	n-Heptane

* In this optically accessible diesel engine, one of the two exhaust valves of the production cylinder head is replaced by a window and periscope.

The optical engine is a single-cylinder version of the heavy-duty diesel Cummins N-series (13.97/15.24 cm bore/stroke). The engine is equipped with a Bowditch piston with a right-cylindrical bowl and a flat piston-crown window providing imaging access to the bowl, viewing from below. A flat, round window is also installed in place of one of the exhaust valves for imaging access to a portion of the squish region above the piston (view not used in the current study). A 30-mm wide curved window matching the contour of the bowl-wall allows laser access into the bowl. Flat rectangular windows installed in a ring at the top of the cylinder provide additional laser access through the cylinder wall. Information about engine geometry is in Table 1 and a schematic of the experiment is in Figure 1. Further details about this engine can be found in Refs. [21,22].

The fuel is high purity n-heptane (≥99% from SIGMA-ALDRICH, for HPLC). Compared to U.S. diesel fuel, the cetane number of 56 for n-heptane [23] is slightly higher than the value of 44 typical of U.S. diesel fuel [24]. It also has a lower density, a much lower boiling point, and zero aromatics. With only a slightly higher cetane number, the auto-ignition characteristics of these two fuels are similar. The lower boiling point means that the liquid-to-vapor transition in the fuel jet will occur sooner. While the absence of aromatics will likely shift the threshold and reduce the amount of soot formation, the general in-cylinder mechanisms of post-injection interactions with in-cylinder soot formation and oxidation should be similar [25].

As described in detail in the following section, the horizontal laser sheets for the optical diagnostics enter from the right of the schematic in Figure 1, passing through both the cylinder-wall window and the bowl-rim window. While the cylinder-wall window is not curved, the bowl-rim window is curved, with concentric surfaces, so that it is a negative cylindrical lens. Hence, when the laser sheet passes through the bowl-rim window, its divergence in the horizontal plane increases somewhat. Also, the laser sheets were oriented parallel to the firedeck, while the nominal jet axis is declined 12° from the firedeck. Hence, the sheet intersects the jet at a 12° angle relative to the jet axis so that the soot-PLII images are not on a nominal symmetry plane of the jet.

As specified in Table 1, the injector is a centrally mounted solenoid-actuated common-rail (CR) Delphi DFI 1.5 with eight 131-micron orifices, equally spaced with an included angle of 156°. Because of the low lubricity and low viscosity of special fuels (such as n-heptane) selected for optical research, the production CR fuel pump could not be utilized. Instead, a custom high-pressure diaphragm pump specially designed for low-lubricity fuels pressurizes the fuel rail at up to 2000 bar. The delivery rate of the diaphragm pump is limited, however, and as a result it could only sustainably pressurize the fuel rail to at most 1200 bar at the designed static back-leak rate of this particular injector.

Optical Setup

As shown in Figure 1, PAH and soot are probed simultaneously by two different color laser-beam sheets, and two intensified charge-coupled device (ICCD) cameras image the soot-PLII and PAH-PLIF signals. As specified in Table 2, PAH-PLIF is excited at three different laser-light wavelengths of 355-, 532-, and 633-nm to probe the growth of PAHs. The 1064-nm laser is for soot-PLII, which is not expected to generate any measurable PAH fluorescence signal. Only one PAH-PLIF laser is used at a time, spatially combined with the soot-PLII laser in front of the cylinder window. For all but 633-nm excitation, the two lasers are both Q-switched Nd:YAG lasers operating at 10 Hz and with pulse durations of approximately 10 ns. Since 633 nm is not a wavelength that Nd:YAG laser can directly provide by frequency doubling/tripling, a Spectra Physics MOPO model optical parametric oscillator (OPO) converts 355 nm Nd:YAG laser light to 633 nm. When operating the Nd:YAG laser either with or without the OPO, the beams are attenuated to ~70 mJ/pulse outside the engine at all three PAH-PLIF excitation wavelengths using a λ/2 plate and polarizer. The 1064-nm soot-PLII beam is similarly attenuated to 250 mJ/pulse outside the engine. The soot-PLII and PAH-PLIF beams are spatially overlapped as shown in Figure 1. The overlapped laser beams are reshaped to 12-mm wide horizontal sheets at an elevation of 14 mm below the cylinder-head firedeck. Temporally, the 1064-nm soot-PLII laser pulse is 2.5 microseconds later than the PAH-PLIF laser pulse, which is long enough to avoid any signal cross-talk but is still effectively simultaneous relative to engine fluid-mechanical and chemical timescales.

As shown in Figure 1 and as listed in Table 2, a PI-MAX 3 HQf ICCD camera captures the PAH-PLIF images, and a PI-MAX 3 SB ICCD captures the soot-PLII images. Both ICCD intensifiers use the same model of camera lens, a Nikkor f/2.5 with 105-mm focal-length. As shown on the lower part of the schematic in Figure 1, a beamsplitter directs the PAH-PLIF and soot-PLII signals to the two cameras. Details of the beamsplitter are deferred to a later paragraph, after the spectral filters or the various diagnostics are described.

In addition to the desired PAH-PLIF and soot-PLII signals, other sources of interference are also present. Foremost is the potential for elastic scatter off in-cylinder surfaces illuminated by the PAH-PLIF laser beam. To reject such elastic scattering interference from the PAH-PLIF laser, as well as to protect the camera intensifier photocathode from damage, a XNF-532 or XNF-633 laser-line notch-filter is placed in front of the PAH-PLIF camera intensifier when using either 532- or 633-nm laser excitation, respectively, as listed in Table 2. For 355-nm PAH PLIF, a long-wave-pass (LWP) color-glass filter with a cut-off near 395 nm (GG-395) effectively blocks the laser elastic scatter while transmitting PAH fluorescence emission, such that a notch filter is not required. Likewise, a laser-line notch filter is not required for the soot-PLII camera because other edge filters effectively block the laser elastic scatter, as described below. To protect the PAH-PLIF camera intensifier photocathode from strong laser elastic-scatter of the soot-PLII 1064-nm beam, an 850-nm short-wave-pass (SWP) filter is also added to the PAH-PLIF filter pack. A SWP-850 filter is not required to protect the soot-PLII camera, as its spectral filter pack effectively blocks 1064-nm laser elastic-scatter.

A second source of interference is the combustion natural luminosity, which is primarily broadband incandescence from soot, and may also include significant chemiluminescence from various sources. The intensity of natural luminosity from soot and other emission sources is relatively weak compared to the laser-induced emissions [26], but they emit for a much longer duration, so short intensifier gates must be utilized to minimize interference from natural luminosity. Hence, in addition to the spectral filtering described above, to further minimize the broadband natural luminosity background, the intensifiers of both ICCD cameras are set to their respective minimum gate durations, 2.54 ns for PAH-PLIF and 275 ns for soot-PLII. Though the typical lifetime of the laser-induced fluorescence signal is longer than 2.54 ns [26], the signal-to-noise ratios (S/N) of the PAH-PLIF images are highest when using this short gate. Since the soot-PLII camera is collecting over a shorter wavelength range, where natural luminosity is much weaker than in the longer

wavelength range [26], the 275 ns minimum gate is short enough for acquiring acceptable S/N soot-PLII images, especially at the lower intake-O_2 conditions tested. The intensifier gain is set to 80% of maximum linearized gain for both cameras. This setting avoids significant pixel saturation on the selected data collecting time but is sensitive enough to utilize most of the available dynamic range.

As listed in Table 2, the soot-PLII emission is filtered to short visible wavelengths from 385 to 450 nm by a LWP color-glass filter with a cut-off near 385 nm (GG-385) and a SWP filter with a cutoff near 450 nm. These short wavelengths are utilized for the soot-PLII diagnostic because the S/N of the laser-heated soot within the laser sheet relative to the combustion-heated soot along the entire camera line-of-sight is higher at shorter wavelengths.

The type of beamsplitter that directs the PAH-PLIF and soot-PLII signals to the two cameras depends on which combination of diagnostics is used. For PAH-PLIF with 633- or 532-nm laser excitation, the PLIF signal collection range (465-850 nm) doesn't overlap with the PLII signal (385-450 nm). Hence, a LWP dichroic mirror with a cut-off near 465 nm is sufficient to separate the two signals efficiently. This LWP dichroic beamsplitter also enforces the lower end of the 465-850 nm collection range for 532- and 633-nm PAH-PLIF. For 355-nm PAH-PLIF excitation, however, the PAH-PLIF signal spectrally overlaps with the soot-PLII signal. Consequently, instead of a dichroic mirror, a 50/50 broadband beam splitter divides the laser-induced emissions equally between the 355-nm PAH-PLIF and soot-PLII cameras.

Table 2: Specifications of PAH-PLIF and soot-PLII diagnostics

Diagnostic	PAH-PLIF	PAH-PLIF	PAH-PLIF	soot-PLII
Laser [nm]	355	532	633	1064
PAH rings	2-4 (small)	4-8 (medium)	10+ (large)	Soot
Camera	PI-MAX3 HQf			PI-MAX3 SB
Camera lens	Nikkor 105 mm, f/2.5			
Intensifier gate [ns]	2.54			275
Spectral Filters	GG-395 SWP-850	XNF-532.0 SWP-850	XNF-632.8S WP-850	SWP-450 GG-385
Detection Range [nm]	395-850	465-850 (- 532 notch)	465-850 (- 633 notch)	385-450
Beamsplitter	50-50 broadband	LWP 465 dichroic	LWP 465 dichroic	as PAH-PLIF
Laser pulse energy [mJ]	~70	~70	~70	~250

As shown in the top view of the piston in Figure 2, a quartz window installed in the piston bowl-rim at the 3 o'clock position is aligned with the window in the cylinder wall, which provides laser-sheet access into the piston bowl when the piston is near top dead center (TDC). Since the injector holes are equally-spaced and the engine has low swirl (0.5 swirl number), the jets are close to symmetric, according to previous studies on this setup. Hence, the one jet of eight that is probed by the laser in the field of view as indicated in Figure 2 is taken as representative of the other seven jets. The images shown later in the Results and Discussion section are all from this region indicated in Figure 2.

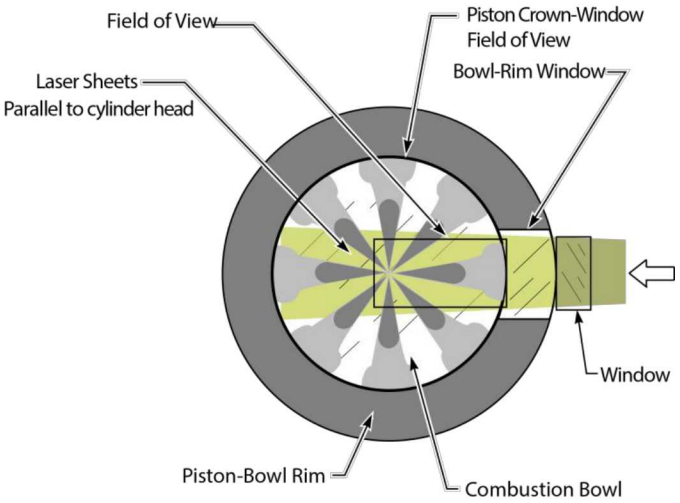

Figure 2: Schematic showing top view of piston bowl with spray and jet orientations relative to the horizontal laser sheet, bowl-rim window, and the imaging field of view.

Engine Operating Conditions

As described in the introduction, the aim of this work is to better understand soot and PAH formation in diesel engines by using a threshold-sooting condition where formation is expected to dominate oxidation. Two primary variables are swept: intake-O_2 mole-fraction (i.e., dilution) and CR fuel-pressure, as specified in Table 3. The operating conditions are selected to match engine combustion network (ECN) conditions, with estimated motored TDC core-gas conditions of 22.8 kg/m^3 and 900 K. Based on isentropic compression calculations using the measured cylinder pressure, the intake temperature and pressure required to achieve these TDC conditions are 110º C and 220 kPa for all conditions. The engine operates at 1200 RPM, which aligns well with the 10-Hz pulse rate of the Nd:YAG lasers and allows one laser pulse per engine cycle. The engine is skip-fired to avoid excessive temperature gradients within the windows that could cause them to break. For each experimental test run of 40 fired cycles, each fired cycle is followed by nine motored cycles.

Here, low intake-O_2 mole-fraction is achieved though dilution with N_2.[*] To determine an appropriate intake-O_2 mole-fraction that yields a threshold-sooting condition, the intake-O_2 mole-fraction is swept from 7.5% to 15.0%, as listed in Table 3. As will be described in the results section, at the mid-range CR fuel-pressure of 800 bar, an intake-O_2 mole-fraction of 10.0% yielded threshold soot-PLII and easily observable PAH-PLIF, while 9.0% intake-O_2 yielded only PAH-PLIF. Additionally, the 9.0% intake-O_2 condition at 533-bar CR fuel-pressure produced no detectable 633-nm PAH-PLIF or soot-

[*] In a practical engine, the diluent would be burned gases via EGR, which would mean higher CO_2 and H_2O would change the in-cylinder charge-gas properties, and hence the compressed-gas density and temperature. These thermodynamic effects, along with possible chemical effects of CO_2 and H_2O and other products of combustion, would likely shift the O_2 mole-fraction thresholds of PAH and soot formation.

PLII. Hence, 9.0% intake-O_2 and 800-bar CR fuel-pressure is taken as the dilution and CR fuel-pressure threshold of PAH/soot formation.

As specified in Table 3, all engine operating conditions use a duration of solenoid energizing (DSE) of 4 ms, and a start of solenoid energizing (SSE) time of 347 crank-angle degrees (CAD), with 360 CAD defined as TDC of the compression stroke. Considering the hydraulic and electro-mechanical delays of the injector, the start of injection is near 350 CAD, and the end of injection is near 380.5 CAD. The CR fuel-pressure is varied by a factor of 1.5 times higher and lower than the 800-bar base condition, or 1200-bar and 533-bar, respectively. With a constant DSE, the engine load increases with CR fuel-pressure as specified in Table 3 according to the gross indicated mean effective pressure (IMEPg) for each condition. While load can affect in-cylinder temperatures, analysis in the Results and Discussion section shows that this load change has a negligible effect on the gas temperatures when PAH and soot are initially forming.

Table 3: Engine operating conditions and diagnostics employed for intake-O_2 and CR fuel-pressure sweeps

	P_{rail} [bar]	533	800	1200
7.5% O_2	**PAH-PLIF [nm]**		633	
	IMEP [kPa]		396	
9.0% O_2	**PAH-PLIF [nm]**	633	355, 532, 633	633
	IMEP [kPa]	449	582	690
10.0% O_2	**PAH-PLIF [nm]**		355, 532, 633	
	IMEP [kPa]		666	
12.5% O_2	**PAH-PLIF [nm]**		355, 532, 633	
	IMEP [kPa]		778	
15.0% O_2	**PAH-PLIF [nm]**		633	
	IMEP [kPa]		817	
CR SSE, [CAD]		347		
CR DSE, [ms]		4		
Engine Speed, [RPM]		1200		
IMEPg [kPa]		396-817 (see rows above)		
Skip fire ratio		1:9 (1 fired followed by 9 motored cycles)		
Intake temperature, [°C]		110		
Intake pressure, [kPa]		220		
Estimated TDC temperature, [K]		900		
Estimated TDC density, [kg/m^3]		22.8		

For the operating conditions with intake-O_2 mole-fractions lower than 12.5%, PAH-PLIF and soot-PLII images are acquired over a span of 18 degrees crank angle (°CA), with one frame every 2 °CA, starting at 364 CAD. This 18-°CA span is long enough to cover the start of PAH formation through to soot formation, if there is any. At least 12 images are recorded at each CAD timing, one per cycle. The conditions with intake-O_2 mole-fractions of 12.5% or higher burn faster and form more soot, so a shorter span of 10 °CA and 2 °CA (0.5 °CA resolution) are covered for 12.5% and 15.0% intake-O_2 mole-fraction conditions, respectively.

Results and Discussion

As described in the introduction, our current understanding of the progression of PAH to soot is that it starts with small PAH (355-nm PAH-PLIF), which grows to medium PAH (532-nm) and then to large PAH (633-nm), and finally to soot (soot-PLII). According to the objective to study threshold soot-formation, we focus mostly on the results of the "final" PAH stage of large PAH excited at 633 nm, along with soot-PLII using the 1064-nm laser beam. At the end of this Results and Discussion section, we present images of other size-classes of PAH from 355- and 532-nm excitation.

Effects of Dilution on Large PAH and Soot

The ensemble-averaged 633-nm PAH-PLIF and soot-PLII images at 7.5% intake-O_2 mole-fraction and 800 bar CR fuel-pressure are shown in Figure 3. The white circle at the left of each image indicates the injector tip, and the white curve on the right edge represents the piston bowl-wall (see Figure 2 for camera field of view). The laser-sheet enters from the right, and propagates from right to left. The image acquisition timing is indicated on the upper left corner of each frame, in CAD. For each frame, the PAH-PLIF signal is false-colored green, and soot-PLII is false-colored red. The false-colored pixel intensity has been rescaled with zero at the 800-count black level of the raw images to full scale at half of the maximum counts on each frame (65,536 counts is the full raw-image bit-depth). While some information is contained the in the signal intensity, the uncertainties are considerable, and include quenching, fluorescence yield and spectral distribution of different PAH species, laser attenuation, signal trapping, and other interference sources. Hence, quantitative information about PAH or soot concentration cannot be derived from the signal intensity.

No PAH-PLIF signal (green) is present in Figure 3, though some signal is present in the soot-PLII images (red). This soot-PLII signal is due to two likely sources, neither of which are soot at this operating condition. First, apparent scattering signal from five liquid sprays emanating from the injector is observable on the left side of most images. Based on previous observations of laser-induced broadband 'flare' originating from the intersection of the laser sheet with in-cylinder surfaces [27], we deem it likely that the intersection of the 250 mJ laser sheet with the inner wall of the piston bowl opposite the bowl-rim window (to the left in the images, outside the field of view) is generating broadband flare that reflects off the liquid spray. Being broadband, the flare is not fully rejected by the spectral filter in front of the camera lens. Furthermore, this incidental illumination of the sprays by laser flare (and potentially by other sources) is not controlled in any way, such that the strength of this scattering interference may not be uniform among all of the sprays. For example, the horizontal (3-o'clock) spray is dimmer than the other sprays in the images in Figure 3. This weaker scattering interference does not imply that the horizontal spray is any different than the other sprays; only that the flare created outside and to the left of the field of view of the images does not illuminate all of the sprays uniformly. When more soot is formed and absorbing the 1064 nm laser beam, this liquid-scatter interference is considerably weaker, especially relative to the soot-PLII signal, and hence is not as visible in later images due to the greater intensity scaling in those images. Second, the bright spots to the right of the injector in some images are likely incandescence and/or scattering interference from particles abraded off the piston rings, which appear randomly in a fraction of images, and appear more pronounced due to ensemble-averaging.

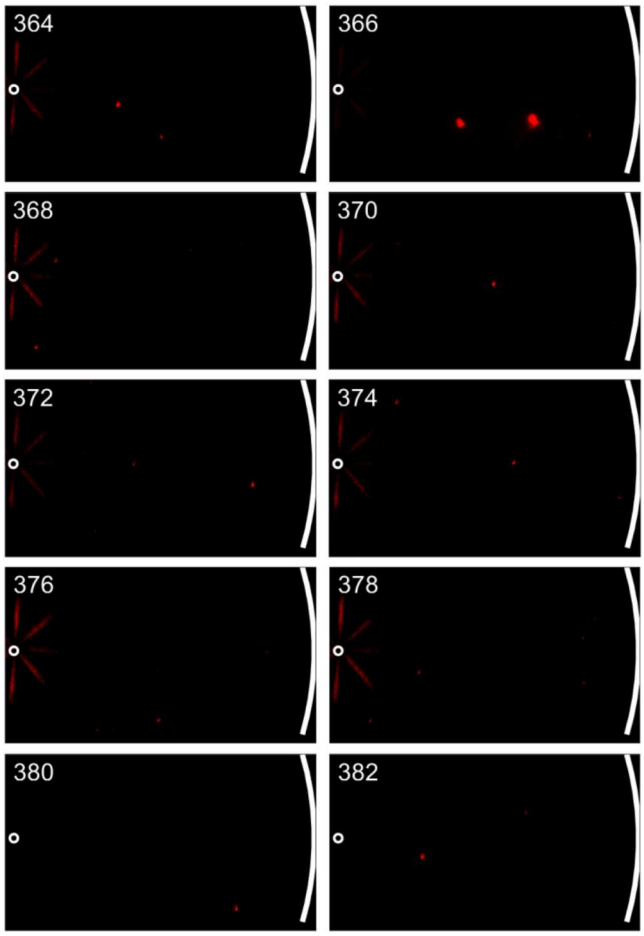

Figure 3: Composite images of ensemble-averaged 633-nm PAH-PLIF (false-colored green) and soot-PLII (red) with 7.5% intake-O_2 and 800-bar CR fuel-pressure. The CAD of image acquisition is shown in the upper left corner of each image.

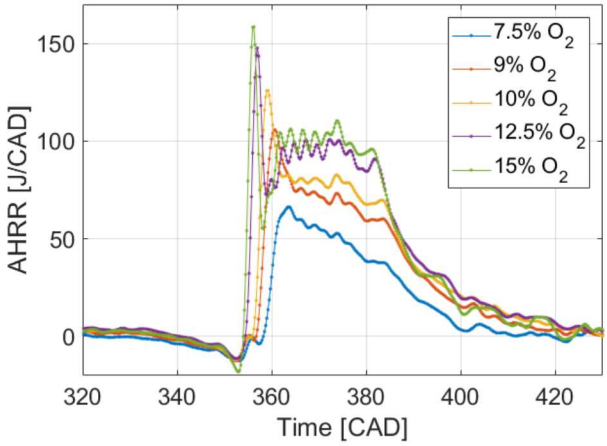

Figure 4: Apparent heat release rate for a sweep of intake-O_2 mole-fraction at 800-bar CR fuel-pressure (see Table 3 for operating conditions).

According to the apparent heat release rate (AHRR) data shown in Figure 4, ignition and combustion occur within the imaging range from 364 to 382 CAD for 7.5% intake-O_2 mole-fraction, so if PAH or soot were formed, they should be visible in the images. At this condition, the high level of dilution presumably yields post-combustion temperatures that are too low for large PAH or soot formation [11].

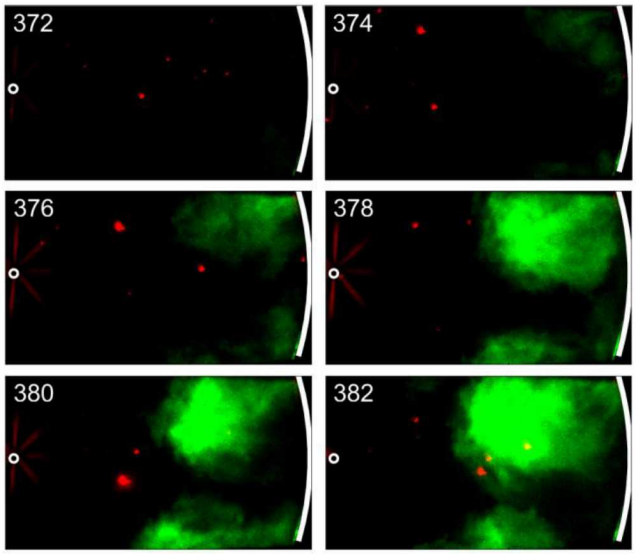

Figure 5: Composite images of ensemble-averaged 633-nm PAH-PLIF (false-colored green) and soot-PLII (red) with 9.0% intake-O_2 and 800-bar CR fuel-pressure. The CAD of image acquisition is shown in the upper left corner of each image.

Figure 5 shows the ensemble-averaged results for 9.0% intake-O_2 mole-fraction and 800-bar CR fuel-pressure. The imaging data are acquired from 364 to 382 CAD, but images acquired before 372 CAD have no meaningful signal (i.e., they are similar to corresponding images in Figure 3), and are not presented in Figure 5.

For the 9.0% intake-O_2 condition in Figure 5, the start of combustion in Figure 4 is 3 ºCA earlier than for the 7.5% intake-O_2 condition, the premixed burn spike is larger, and the integrated heat release and load are higher. At 372 CAD, true soot-PLII is not yet present – only broadband scattering and other isolated particle interference are visible in red. Appreciable 633-nm PAH-PLIF initially appears at 374 CAD, in the downstream jet-jet interaction region between neighboring jets. No significant PAH-PLIF is observed near the jet axis in the free-jet region between the injector and the piston bowl-wall, i.e., prior to jet impingement on the bowl-wall. Thereafter, from 376 to 380 CAD, the PAH-PLIF region grows in both size and brightness.

This observation of prominent PAH in the jet-jet interaction region might be explained by the local equivalence ratio distribution, which is likely lower in the downstream region of the jet where the rich air/fuel mixture meets fresh ambient air in the jet-jet interaction region. Since PAH formation is sensitive to temperature [28], PAH is expected to form first in regions that are sufficiently hot, which apparently includes the jet-jet interaction region, but not the richer jet axis. After it ignites in the jet-jet interaction region, the leaner downstream region (though still fuel rich) may have higher combustion temperatures which may promote additional PAH formation downstream rather than in cooler, upstream regions on the jet axis, which also have a shorter residence time. After the injection ends near 380.5 CAD, combustion typically flashes back to the injector, and the upstream temperature may increase, which may

promote PAH formation farther upstream and closer to the jet axis, as evident at 382 CAD. Hence, for both the 7.5% and 9.0% intake-O_2 conditions, no soot-PLII is observed, and PAH-PLIF is only present for the 9.0% intake-O_2 condition.

Figure 6 shows the ensemble-averaged 633-nm PAH-PLIF and soot-PLII images with 10.0 % intake-O_2 and 800 bar CR fuel-pressure. Figure 4 shows that the start of combustion is further advanced compared to the 7.5% and 9.0% intake-O_2 conditions, and the premixed burn spike, integrated heat release, and load are also higher. The PAH-PLIF signal is first apparent at 368 CAD, which is 6 °CA sooner than for the 9.0% intake-O_2 condition. The PAH-PLIF signal also first appears close to the piston bowl-wall, and more in-line with the nominal jet axis, rather than off to the sides of the jet axis in the jet-jet interaction regions as for the 9.0% intake-O_2 condition in Figure 5. By 372 CAD, more PAH-PLIF signal is apparent in the jet-jet interaction region, and soot-PLII signal first appears. The PAH-PLIF intensity increases at 374 CAD, though the spatial extent of the PAH-PLIF is similar to that for 372 CAD. At 372 and 374 CAD, the soot appears on the edge of PAH cloud and overlaps slightly (yellow color due to combination of red and green) with PAH even in these ensemble-averaged images, indicating that this relationship is repeatable. After 374 CAD, more PAH-PLIF signal appears farther from the bowl-wall, and fuel is still being injected through the end of the sequence at 378 CAD. Soot formation is restricted to the periphery of the jet-jet interaction region. In the latter images, a thin ribbon of soot exists at the edge of PAH cloud and overlaps with PAH slightly. In this region, where fuel-rich mixtures likely meet the surrounding ambient air at the diffusion flame [1], the highest temperatures should exist near the stoichiometric contour. Only near this diffusion-flame region, temperatures may be above the soot-formation threshold, hence the limited region where soot is observed.

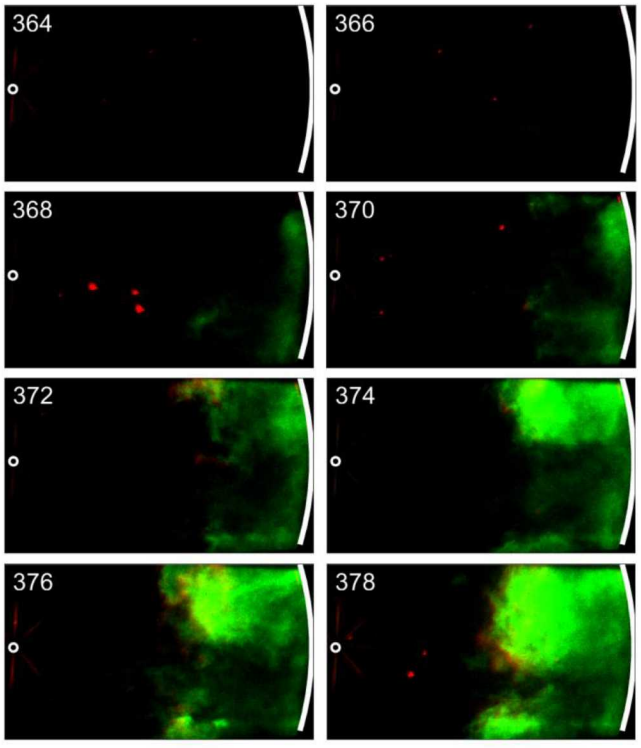

Figure 6: Composite images of ensemble-averaged 633-nm PAH-PLIF (false-colored green) and soot-PLII (red) with 10.0% intake-O_2 and 800-bar CR fuel-pressure. The CAD of image acquisition is shown in the upper left corner of each image.

In Figure 7, the 12.5% intake-O_2 and 800 bar CR fuel-pressure condition, 633-nm PAH-PLIF signal first appears at TDC, in-line with the jet axis, in the downstream jet near the piston bowl-wall. The initial PAH-PLIF signal appears 6 °CA (~1.1 ms) sooner than for the 10.0% intake-O_2 mole-fraction case, and the start of combustion in Figure 4 is also advanced by 2 °CA relative to the 10.0% intake-O_2 condition. Similar to the 10.0% intake-O_2 condition, soot is first apparent on the edge of PAH cloud at TDC, and in the same image as the first PAH at 360 CAD, though only a small amount of soot-PLII is present. Unlike the 10.0% intake-O_2 condition, starting at 362 CAD, the spatial extent of the soot increases dramatically both outside and toward the center of the PAH-PLIF cloud, though soot doesn't extend completely to the center of the PAH cloud in these ensemble-averaged images. The spatial extent of the PAH-PLIF signal doesn't increase much at 362 CAD, but the signal intensity increases markedly. Much more yellow soot-PAH overlap is apparent starting at 362 CAD than for the 10.0% intake-O_2 condition. In the latter ensemble-averaged images, the spatial extent of the PAH-PLIF signal doesn't change much, but the soot-PLII intensity decreases at 366 CAD, especially outside of the ensemble-averaged PAH cloud.

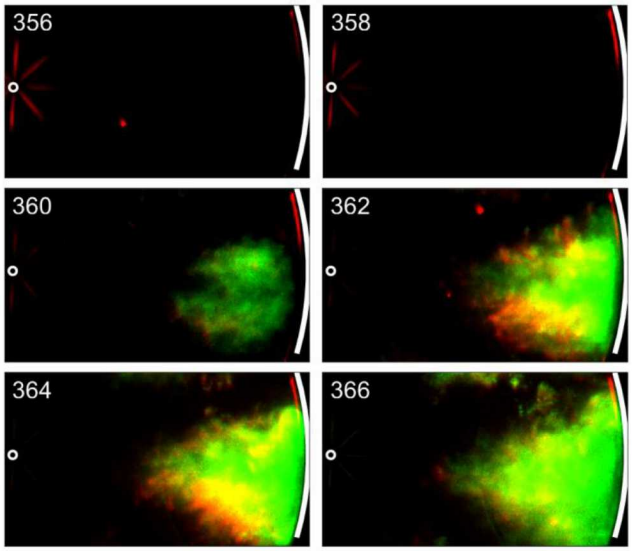

Figure 7: Composite images of ensemble-averaged 633-nm PAH-PLIF (false-colored green) and soot-PLII (red) with 12.5% intake-O_2 and 800-bar CR fuel-pressure. The CAD of image acquisition is shown in the upper left corner of each image.

While ensemble-averaged images are useful for portraying the statistically averaged PAH and soot distributions, they do not necessarily represent the true physical relationships, including the extent of overlap, especially when cycle-to-cycle variations in the PAH and soot distributions are large. Here, the single-shot instantaneous PAH-PLIF and soot-PLII distributions are not as symmetric about the jet axis as the ensemble-averaged images appear, and cycle-to-cycle variation is considerable as well. Hence, the true spatial relationships that affect relevant physical and chemical processes are better represented by instantaneous single-shot images. As described earlier in the Optical Setup subsection, the PAH-PLIF and soot-PLII images for each cycle are effectively recorded simultaneously, and these simultaneous single-shot images

are more representative of the true PAH/soot overlap. Combined and contrasted with the ensemble-averaged data, the single-shot images provide additional useful information.

Figure 8 shows two sequences of selected single-shot composite PAH-PLIF and soot-PLII images at each imaging CAD for the same 12.5% intake-O_2 engine operating condition as in Figure 7. Although individual images are presented in series with increasing CAD, each composite image is from a different engine cycle. There is no direct temporal connection among any of the composite images. Like the ensemble-averaged images in Figure 7, the PAH-PLIF signal (green) in the instantaneous images of Figure 8 appears at 360 CAD and generally grows brighter and spatially larger by 362 CAD. Thereafter, the soot-PLII signal (red) generally appears on the periphery of the PAH-PLIF region, and overlaps (yellow color) with PAH-PLIF to a lesser degree than portrayed in ensemble-averaged images in Figure 7. Comparing the soot-PLII signal distributions and brightness for each pair of images, considerable cycle-to-cycle variations are evident, and the trends are not monotonic in time (CAD) for these instantaneous images from separate cycles. The minimal overlap of PAH-PLIF and soot-PLII is consistent in the single-shot images, however, compared to the much greater overlap in the ensemble-averaged images of Figure 7.

The extent of overlap in the soot and PAH is important for developing understanding of soot formation processes, both for conceiving strategies to mitigate soot formation and to improve computer simulation fidelity through submodel development. Two important contributors to the apparent overlap in the images are the actual physical overlap of soot and PAH, as well as cross-talk between the two diagnostics. Given that the soot-PLII diagnostic uses an infrared laser beam at 1064 nm, it is unlikely that it will either be absorbed by PAH or that any subsequent fluorescence would be blue-shifted to the 385-450 nm collection band of soot-PLII camera. Consequently, it is unlikely that any signal from PAH-PLIF is present in the soot-PLII imaging data. More conceivable is that the PAH-PLIF beam could induce incandescence of the soot particles in the same way that the 1064-nm beam does for the soot-PLII diagnostic. The instantaneous images in Figure 8 show evidence that such soot-PLII interference in the PAH-PLIF images are unlikely, however. Visual inspection reveals numerous local red-colored areas with strong soot-PLII without any overlap of PAH-PLIF. This indicates that regions where strong soot-PLII signal is present do not also appear with significant intensity as interference in the PAH-PLIF images. It is possible that attenuation of the PAH-PLIF laser beam by soot prevents illumination of soot farther from the laser, or 'down-beam,' but numerous examples in the instantaneous images show PAH-PLIF down-beam of soot-PLII i.e. the white circled regions in Figure 8.

In an effort to quantify the amount of overlap, Figure 9 plots the number of overlapped pixels for either the ensemble-averaged images of Figure 7 or the full set of single-shot images that contributed to the ensemble-averaged images, some of which are included in Figure 8. To quantify the number of overlapped pixels, the PAH-PLIF and soot-PLII images are binarized, with a threshold set to the greater of either 1500 counts or 25% of the maximum intensity in the image. For instantaneous images, the number of overlapped pixels in each image is plotted as averages over all 12 images acquired at each CAD. The overlapped pixels for the ensemble-averaged images are calculated directly from the images in Figure 7. Both datasets peak at 364 CAD, and the number of overlapping pixels at 364 and 366 CAD for the ensemble-averaged images is nearly twice that for the instantaneous images. This provides further quantification of how the overlap in the ensemble-averaged images misrepresents the instantaneous reality.

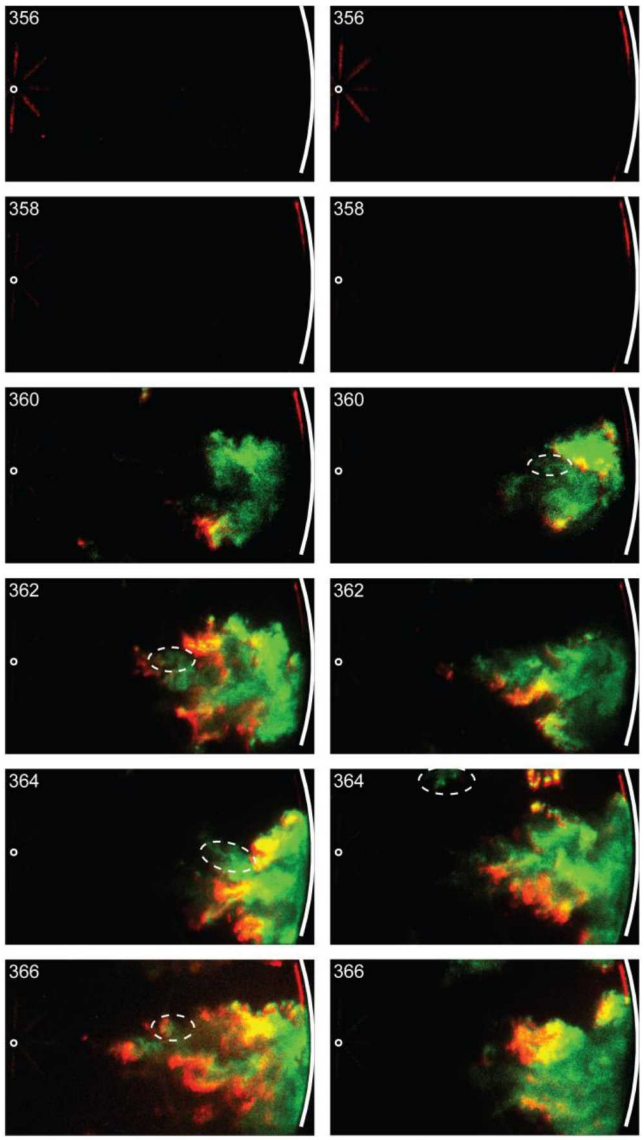

Figure 8: Selected single-shot composite images of 633-nm PAH-PLIF (false-colored green) and soot-PLII (red) with 12.5% intake-O_2 and 800-bar CR fuel-pressure. The CAD of image acquisition is shown in the upper left corner of each image.

For the reasons discussed above, the ensemble-averaged data must be interpreted with care. Many observations reported herein, including the timing and general location (but not overlap) of PAH and/or soot in the ensemble-averaged images, are consistent between the ensemble-averaged and single-shot images, and hence support conclusions based on ensemble-averaged images.

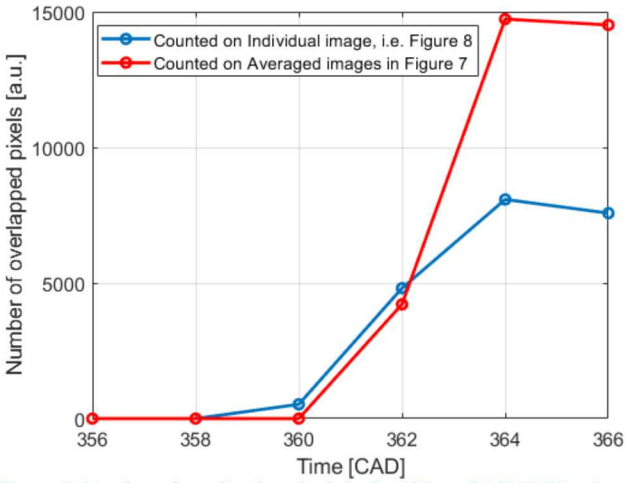

Figure 9: Number of overlapping pixels in the 633-nm PAH PLIF and soot-PLII imaging data contributing to Figure 7 and Figure 8.

Finally, for the highest intake-O_2 mole-fraction of 15.0%, the 633-nm PAH-PLIF and soot-LII imaging data are shown in Figure 10. Only five frames from 356.5 to 358 CAD are presented because both PAH and soot form earlier and grow faster than the other cases. The interval between images in Figure 10 is also only 0.5 °CA, compared to 2 °CA for all imaging data presented prior to Figure 10. This highest intake-O_2 condition has the earliest start of combustion (see Figure 4) and the highest combustion temperature due to less dilution, which consequently promotes soot and PAH formation. Observable PAH-PLIF signal first appears at 356.5 CAD, and 1.0 °CA later, soot-PLII signal appears in the ensemble-averaged images. Comparing the set of ensemble-averaged 633-nm PAH-PLIF and soot-PLII imaging at decreasing amounts of intake-air dilution, the first appearance of large PAH and soot is advanced, and the dwell between them is shortened. Unfortunately, the 2 °CA interval for the images at the 12.5% intake-O_2 condition is too coarse to precisely capture the timing of the initial 633-nm PAH-PLIF and soot-PLII at 12.5% intake-O_2. It is likely that the differential between first apparent of PAH and soot is larger than 1.0 °CA but less than 2 °CA for 12.5% intake-O_2 condition. However, in one of our initial studies of medium-size PAH and soot, we observed that decreasing dilution similarly advances of the onset of 532-nm PAH-PLIF and soot-PLII and shortens the dwell between them [18].

In addition to forming sooner, the large PAH and soot also tend to form farther upstream with increasing intake-O_2 mole-fraction. Furthermore, for the conditions and image timings investigated here, initial soot formation is not observed where the jet impinges on the piston bowl-wall.

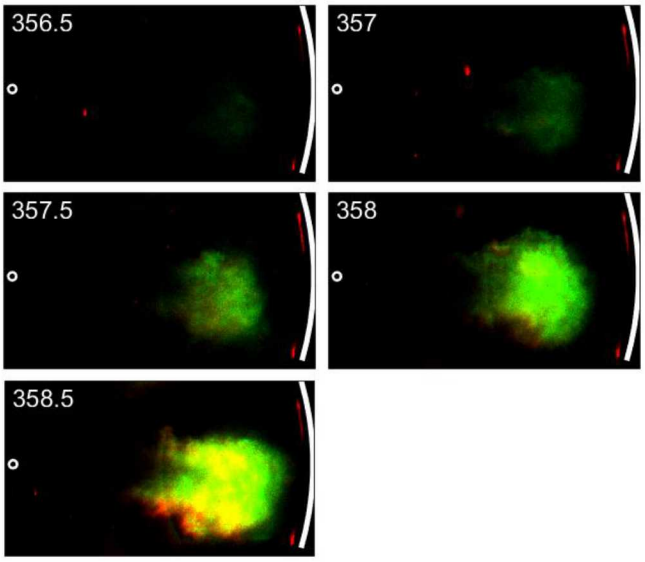

Figure 10: Composite images of ensemble-averaged 633-nm PAH-PLIF (false-colored green) and soot-PLII (red) with 15.0% intake-O_2 and 800-bar CR fuel-pressure. The CAD of image acquisition is shown in the upper left corner of each image.

Effects of CR Fuel-Pressure on Large PAH and Soot

Fuel injection pressure is another key factor for in-cylinder PAH and soot formation. In addition to the 800-bar data presented thus far, two other conditions with CR fuel-pressures a factor of 1.5 higher (1200 bar) and lower (533 bar) were also tested at the same 9.0% intake-O_2 condition as the images in Figure 5. For the 533-bar CR fuel-pressure condition, neither 633-nm PAH-PLIF nor soot-PLII is present in any of the images,[†] which are included in Figure A1 of the Appendix. For the higher CR fuel-pressure, however, 633-nm PAH-PLIF signal appears 4 °CA earlier than the base 800-bar CR fuel-pressure condition, at 370 CAD in Figure 11. Although PAH-PLIF appears earlier, it still forms in the jet-jet interaction regions, similar to the structure observed in Figure 5. Like the images in Figure 5, the region of bright PAH-PLIF grows and extends both upstream toward the injector and laterally toward the nominal jet axis from 372 to 380 CAD. With the higher CR fuel-pressure, soot-PLII signal appears before the end of injection. In the composite images of Figure 11, however, the strong PAH-PLIF signal (green) obscures the weak soot-PLII signal (red) before 380 CAD, such that the weak soot-PLII difficult to discern in Figure 11. Soot-PLII signal is only weakly apparent in the 382 CAD image as dim yellowish pockets embedded within the PAH-PLIF in the ensemble-averaged images. To better illustrate the soot-PLII signal, Figure 12 shows selected instantaneous single-shot composite images of 633 nm PAH-PLIF and soot-PLII; but the soot-PLII signal in all frames have been rescaled to make the first appearing soot-PLII visible. The first apparent of soot can be found as early as 376 CAD, however, it does not always appear among all 12 replicates at 376 and 378 CAD due to cycle-to-cycle variation as shown in Figure 12. Of the 12 replicates at each CAD, soot appears 3, 8, 11 and 12 times at 376, 378, 380 and 382 CAD, respectively.

[†] 532-nm PAH-PLIF shows weak signal at 376 CAD (not shown here), but no 633-nm PAH-PLIF signal appears at any imaged CAD.

Comparing either Figure 11 and Figure 12 (9.0% O_2, 1200 bar CR) or Figure 6 (10.0% O_2, 800 bar CR) to Figure 5 (9.0% O_2, 800 bar CR), it is apparent that increasing either O_2 or CR fuel-pressure from the pre-threshold-sooting condition of Figure 5 leads to initial soot formation. The distribution of the initial soot is also quite similar; decreasing dilution leads to soot on the jet periphery, and increasing injection pressure also leads to soot on the jet periphery. Soot partially overlaps with PAH periphery but extends farther upstream, which is consistent with the previous n-heptane flames [16]. The explanation offered above that the local combustion temperature is only high enough for soot formation at the jet periphery is consistent with the dilution effect, but the similar behavior at higher CR fuel-pressures in the instantaneous images shown in Figure 12 is at first counterintuitive relative to understanding gained from quasi-steady jets.

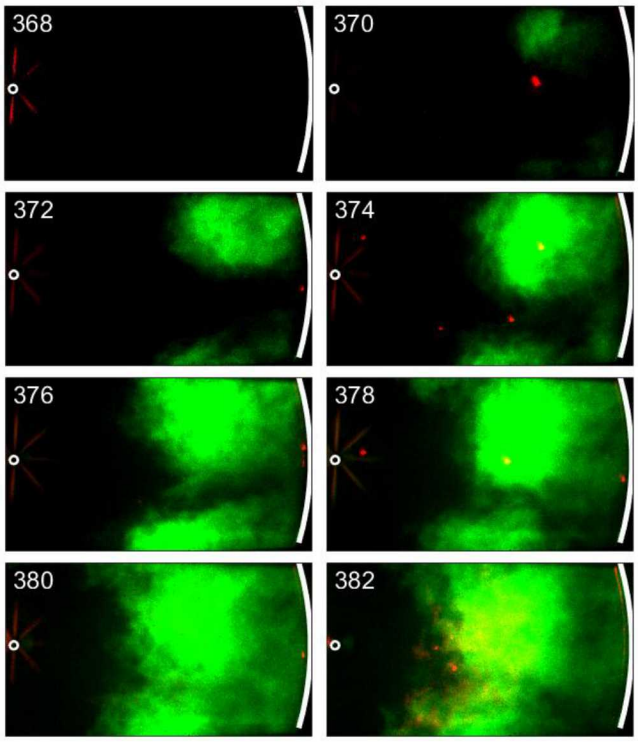

Figure 11: Composite images of ensemble-averaged 633-nm PAH-PLIF (false-colored green) and soot-PLII (red) with 9.0% intake-O_2 and 1200-bar CR fuel-pressure. The CAD of image acquisition is shown in the upper left corner of each image.

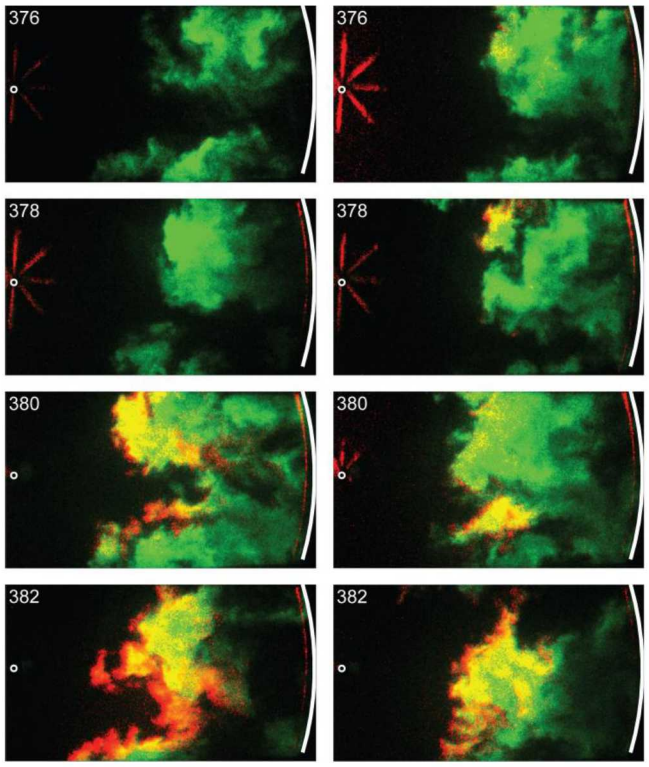

Figure 12: Selected single-shot composite images of 633-nm PAH-PLIF (false-colored green) and soot-PLII (red) with 9.0% intake-O_2 and 1200-bar CR fuel-pressure. The CAD of image acquisition is shown in the upper left corner of each image.

For quasi-steady jets, higher injection pressure increases the lift-off length and entrains more air into the jet upstream of the lift-off length, which yields less soot formation [29]. In contrast, the observation among the three CR fuel-pressure conditions is that PAH forms earlier with higher CR fuel-pressure, and that soot forms in the highest CR fuel-pressure case only. This trend is also contrary to residence-time arguments of previous simplified soot models using a two-stage Lagrangian (TSL) approach [30].

The cause of this apparent contradiction could be due to the effect of temperature on soot and PAH formation at the threshold conditions tested here. As described earlier in the Engine Operating Conditions section, the DSE is held constant, so increasing CR fuel-pressure increases fuel delivery and engine load. Accordingly, the measured peak cylinder-pressure increases with CR fuel-pressure, as shown in Figure A2 of the Appendix. This increase of cylinder pressure should increase the compression-heating of bulk gases entrained into the jet and yield higher temperatures, and could affect soot formation. The load also changes with CR fuel-pressure, given that the injection duration is held constant, and hence more fuel is injected at the higher CR fuel-pressure conditions. The injection duration could be adjusted to maintain load, but this would have little effect on the data reported here because the timing of the initial PAH and soot formation are before the end of injection for all of the conditions. Increasing the injection duration to maintain load at the lower CR fuel-pressure conditions would affect late-cycle and exhaust PAH and/or soot, but these are not within the scope of the current study. Hence, compression-heating effects resulting from changes in the fuel-delivery and consequent heat-release rate with CR fuel-pressure would be virtually identical during the initial PAH and soot formation

period even if the injection durations had been adjusted to maintain load.

To estimate the effects of compression heating among the three CR fuel-pressure conditions, we used a 0-D reacting simulation in Chemkin Pro. In the simulation, equivalence ratio ϕ is set to 2 to represent a mixture near the threshold of soot formation, and the O_2 mole-fraction is 9.0%, as in the experiments. The fuel is n-heptane, and the chemical-kinetic mechanism is from Wang et al. [31]. The measured cylinder-pressure constrains the adiabatic reacting compression simulation for each of the three CR fuel-pressure conditions. Figure 13 shows the temporal evolution of the modeled temperature relative to the time after SOI. The simulated temperature differential from lowest to highest CR fuel-pressure is quite small, about 20 K.

In addition to compression heating due to combustion, the pumping work imparted to the high-pressure fuel is converted to kinetic energy during injection, and ultimately to thermal energy through mixing, which will result in a higher fuel temperature after injection. First-law thermodynamic calculations show that the fuel temperature differential is 25 K between 533 bar and 1200 bar CR fuel-pressure. Once mixed to an equivalence ratio of 2, the resulting temperature increase for the fuel-air mixture is only about 2 K. Hence, in total, the estimated mixture temperature differential is at most about 27 K. Relative to cycle-to-cycle variation during an engine run as the wall temperatures increase, as well as from run-to-run variations during the course of a measurement campaign, this temperature differential seems insufficient for such a repeatable and distinct effect on PAH and soot formation.

This temperature differential is only for an isolated closed-volume, however, and does not account for mixing with hotter regions such as the diffusion flame as would occur in a real turbulent flame. Hence, the local temperature differential with varying levels of turbulent mixing from 533- to 1200-bar CR fuel-pressure could be much larger than the estimated isolated 27-K differential. Indeed, TSL-simulations have shown that higher mixing rates (turbulence) can increase local temperatures on the order of 100 K [30]. Hence the actual temperature differential at the jet periphery where soot forms, and where high temperatures are expected, could be much larger than 27 K from compression-heating alone. Skeen et.al [32] showed that at threshold-sooting conditions, soot formation can vary drastically near a threshold temperature near 1600 K, which is coincidentally similar to the simulated peak compressed-gas temperature for reacting mixtures at and equivalence ratio of 2 in Figure 13.

If these turbulent-mixing temperature differentials are responsible for the transition to soot formation at the highest CR fuel-pressures, then the previously mentioned contradiction with the residence-time arguments of the TSL simulations [30] could be reconciled. The argument about the residence-time effect on PAH and/or soot formation presumes that all different CR fuel-pressure cases always form some amount of PAH/soot. Based on this, increasing CR fuel-pressure decreases PAH/soot formation due to a shorter residence time. However, in the current work, the local temperature of the 533-bar CR fuel-pressure condition may be too low such that large PAH or soot cannot be formed, even though the “residence time” is longer. In the other hand, the 800- and 1200-bar CR fuel-pressure conditions may just cross the PAH/soot forming threshold temperature such that a detectable PAH/soot is formed, even with a shorter residence time.

Regarding the other contradiction, the aforementioned lift-off length explanation works well for quasi-steady jets at conventional diesel conditions, where both soot formation and oxidation are important. In this threshold-sooting condition, soot formation likely dominates oxidation effects, so CR fuel-pressure effects on soot oxidation [33] might not be significant here.

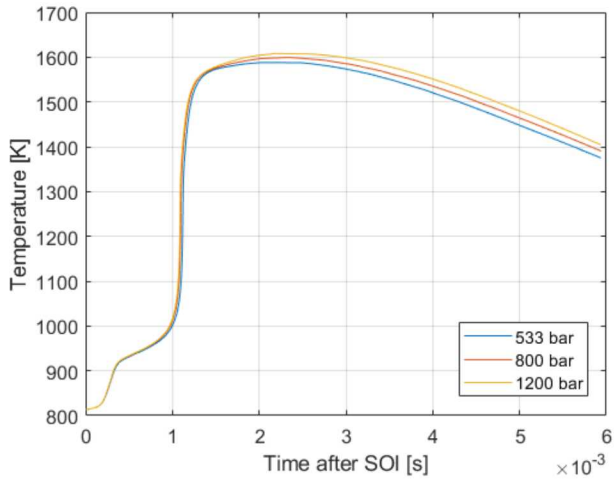

Figure 13: Zero-dimensional closed-volume chemical-kinetic simulations of n-heptane ignition and combustion at an equivalence ratio of 2, for adiabatic compression according to the measured cylinder pressure at three different CR fuel-pressures.

Effects of Dilution on Small and Medium PAH

All of the PAH-PLIF images presented thus far use 633-nm excitation to probe large (10+ rings) PAHs that are expected to form just prior to soot formation. As described in the introduction, smaller PAHs also can be probed using shorter wavelength laser light. This subsection presents soot-PLII and simultaneous PAH-PLIF using two additional shorter laser wavelengths.

Figures 14 and 15 show composite images of PAH-PLIF using 532- and 355-nm excitation respectively, along with soot-PLII using the same 1064-nm excitation wavelength as in other images presented thus far. The engine is operated at the base condition with 9.0% intake-O_2 mole-fraction and 800-bar CR fuel-pressure (also see Table 3). The 355-nm PAH-PLIF signal first appears at 366 CAD (Figure 15), then at 372 CAD for 532-nm PAH-PLIF (Figure 14), then at 374 CAD for 633-nm PAH-PLIF (Figure 5). As described earlier when Figure 5 was presented, soot is not detected at this condition, but for the 10.0% intake-O_2 condition of Figure 6, the soot-PLII signal first appears 4 °CA after the appearance of 633-nm PAH-PLIF signal. Hence, this sequence shows that for these dilute, threshold-sooting conditions, small PAH appear earliest, about 9 °CA after the start of combustion, followed by medium PAH 6 °CA later, then large PAH 2 °CA later, and finally soot (if it were to form) about 4 °CA later. This progression is consistent with current understanding of soot and soot precursor formation, with small PAH forming first, then adding more rings to grow into to larger PAH, and eventually forming soot [28]. In addition to differences in the temporal appearance of the various PAH size-classes, the spatial distributions of the 355-nm PAH-PLIF are quite different than that for the 532- and 633-nm PAH-PLIF images. Since the 355-nm PAH-PLIF forms earlier, the jet has not penetrated as far, so the small PAHs first

appear closer to the jet axis, close to the bowl wall, and later expands into the jet-jet interaction region as the jet continues to penetrate and spread along the bowl wall.

Although the previous paragraph describes the initial appearance of 355-nm PAH-PLIF at 366 CAD, some signal is present earlier in the sequence. At 358 CAD in Figure 15, some weak signal appears in the ensemble-averaged 355-nm PAH-PLIF image, near the right side of the field of view, in the downstream jet. Referring back to the AHRR data in Figure 4, this is at the end of the small first-stage ignition heat-release, and near the start of the larger second-stage ignition heat release. The signal disappears in the next ensemble-averaged image at 360 CAD, and signal does not appear again until 366 CAD. The appearance of relatively weak emission between the first- and second-stage ignition events is consistent with formaldehyde-PLIF, as formaldehyde is one product of the low-temperature combustion of h-heptane, and it would be consumed during high-temperature ignition [34, 35]. Formaldehyde can be excited by the 355-nm laser beam but neither by the 532- nor 633-nm beams, and hence the weak emission appears near 360 CAD only in the 355-nm PAH-PLIF images. The signal present in the 355-nm PAH PLIF images at 366 CAD and later is after the high-temperature ignition, and the signal is considerably brighter than the earlier emission near 358 CAD, which is also consistent with previous observations of bright PAH relative to weaker formaldehyde fluorescence as discerned by spectroscopic imaging [35]. To our best knowledge, no other emission sources other than formaldehyde and PAH are likely emitting upon excitation at 355 nm. Thus, based on the above reasoning, we interpret the 355-nm PAH-PLIF signal at 358 CAD as formaldehyde fluorescence, while other emission at 366 CAD and later is due to fluorescence of small PAHs.

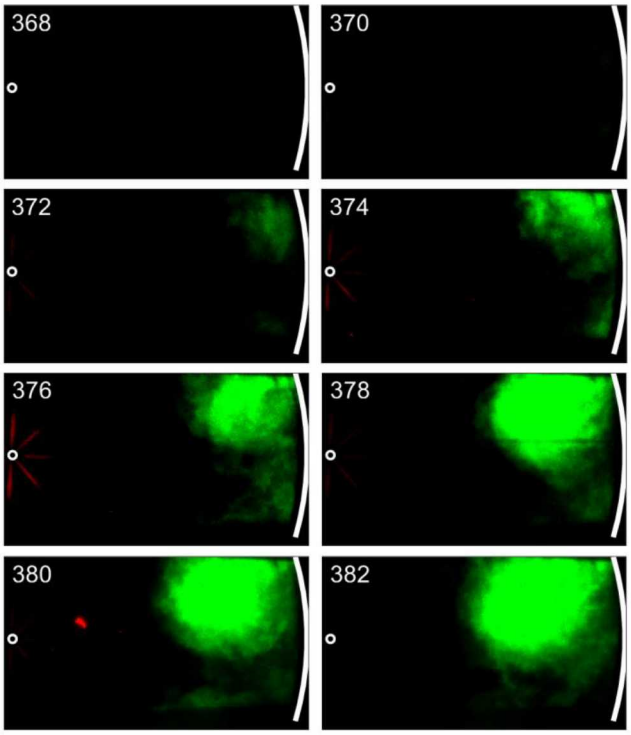

Figure 14: Composite images of ensemble-averaged 532-nm PAH-PLIF (false-colored green) and soot-PLII (red) with 9.0% intake-O_2 and 800-bar CR fuel-pressure. The CAD of image acquisition is shown in the upper left corner of each image.

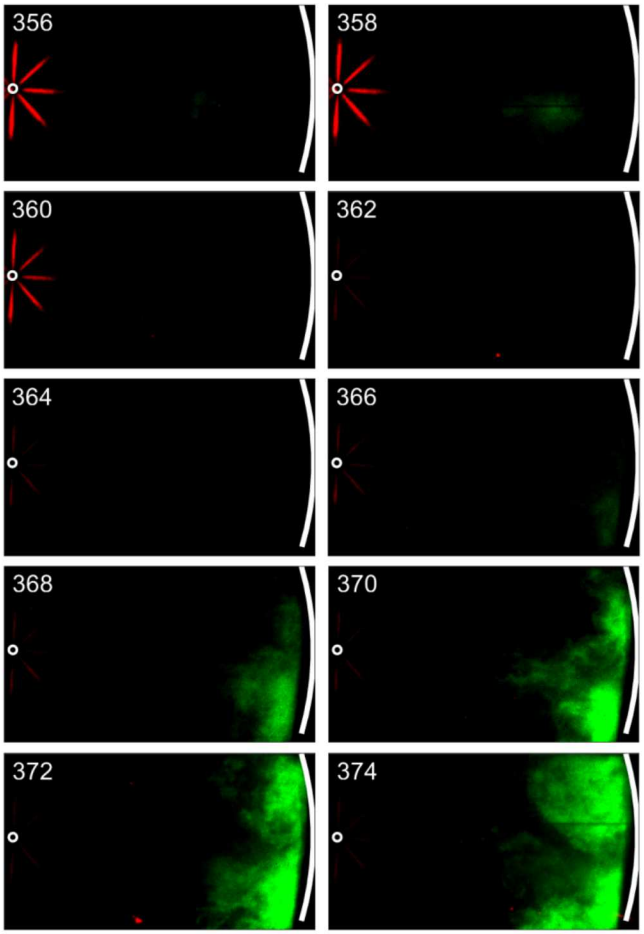

Figure 15: Composite images of ensemble-averaged 355-nm PAH-PLIF (false-colored green) and soot-PLII (red) with 9.0% intake-O_2 and 800-bar CR fuel-pressure. The CAD of image acquisition is shown in the upper left corner of each image.

A few additional intake-O_2 conditions were also tested with 355-nm excitation, and those data are included here as well for reference. Figure 16 and Figure 17 show ensemble-averaged composite 355-nm PAH-PLIF and soot-PLII images for 800-bar CR fuel-pressure with 10.0% and 12.5% intake-O_2 mole-fraction, respectively. Similar to the 9.0% intake-O_2 data in Figure 15, the 355-nm PAH-PLIF appears earlier and/or initially brighter than the 633-nm PAH-PLIF for both 10.0% and 12.5% intake-O_2, though the dwell between 355- and 633-nm PAH-PLIF decreases significantly as the intake-O_2 mole-fraction increases. As the intake-O_2 increases from 9.0% to 10.0% to 12.5%, the dwell between 355- and 633-nm PAH-PLIF decreases from 8 °CA to 4 °CA to ~0 °CA. Also, the spatial distribution of the 355-nm PAH-PLIF shifts upstream in the jet with increasing intake-O_2, moving closer to the nominal jet axis and away from the jet-jet interaction regions. For the 10.0% intake-O_2 condition, comparing PAH-PLIF with 355-nm (Figure 16) and 633-nm (Figure 6) excitation, from 372 to 374 CAD, the large PAHs in Figure 6 appear mostly in the jet-jet interaction region, while the small PAHs in Figure 16 appear closer to the nominal jet axis, and closer to the piston bowl-wall. Additionally, the 355-nm PAH-PLIF signal intensity in Figure 16 decreases from 370 to 374 CAD, especially close to the bowl wall. This could be due to the small PAH being consumed, but more likely it may be due to both increasing attenuation of the 355-nm laser-beam and increasing signal trapping of the small PAH-PLIF signal by soot and PAHs between the laser

sheet and the camera. Similar signal-reduction behavior is observed for the 12.5% intake-O_2 condition in Figure 17, between 364 and 366 CAD, for both PAH-PLIF and soot-PLII, and to an even greater degree. As discussed previously, the 12.5% O_2 mole-fraction condition has significantly stronger soot-PLII signal than the 10.0% intake-O_2 condition. Soot aerosols have broadband absorption with increasing optical density at shorter wavelengths, so the soot should absorb the short-wavelength 355-nm PAH-PLIF signal more than the long-wavelength 633-nm PAH PLIF signal. Indeed, the decrease in the PAH-PLIF signal from 364 to 366 CAD is much greater for 355-nm excitation in Figure 17 (green) than for 633-nm excitation in Figure 7. Furthermore, the soot-PLII signal, which is acquired at relatively short 385-450 nm wavelengths in both Figure 7 and Figure 17, decreases to a similar degree from 364 to 366 CAD.

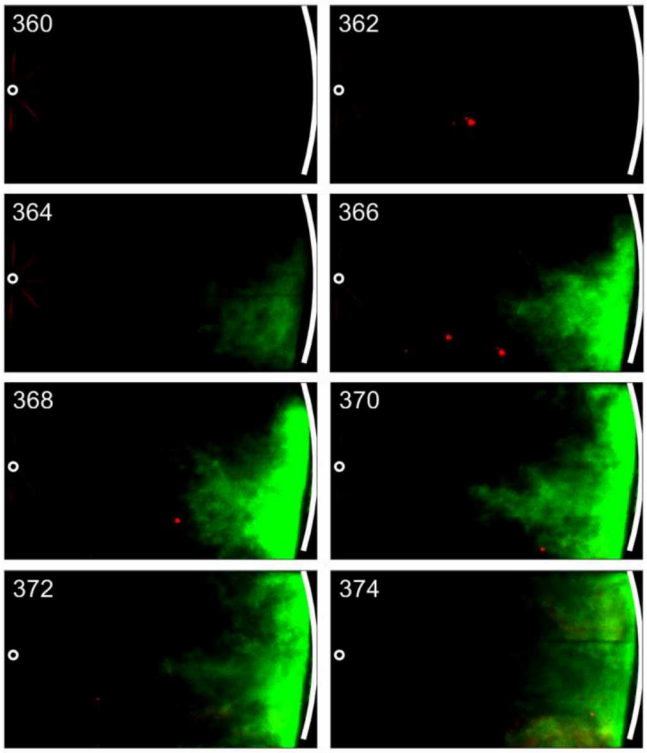

Figure 16. Composite images of ensemble-averaged 355-nm PAH-PLIF (false-colored green) and soot-PLII (red) with 10.0% intake-O_2 and 800-bar CR fuel-pressure. The CAD of image acquisition is shown in the upper left corner of each image.

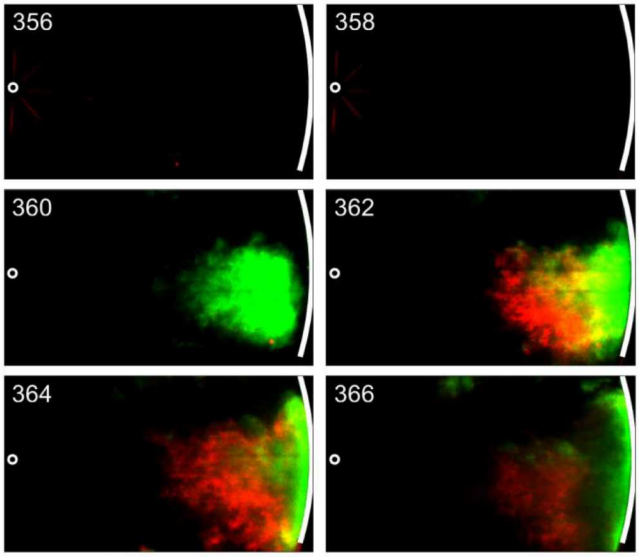

Figure 17. Composite images of ensemble-averaged 355-nm PAH-PLIF (false-colored green) and soot-PLII (red) with 12.5% intake-O_2 and 800 bar CR fuel-pressure. The CAD of image acquisition is shown in the upper left corner of each image.

Considering the discussion above and comparing Figure 7 and Figure 17, the soot-PLII distributions close to the bowl wall are similar (as they should be, since conditions and diagnostics are identical), with a dark region (lack of red or yellow color) on the nominal jet axis and near the piston bowl-wall. This dark region of soot-PLII could be due to signal trapping and/or this center region could be too cold to form soot.

Though signal trapping and/or laser attenuation is likely affecting the 355-nm PAH-PLIF and soot-PLII signals later in the cycle for the 12.5% O_2 mole-fraction condition, the data are nevertheless useful for comparing the initial PAH and soot formation before such effects become important, or in the upstream parts of the jet where signal trapping is likely less severe, as the signal trapping is likely problematic closer to the piston bowl-wall.

Conclusions

This study applies simultaneous PAH-PLIF and soot-PLII to observe PAH and soot formation at various threshold-sooting conditions by altering the intake-O_2 mole-fraction and CR fuel-pressure. Different size-classes of PAH are probed by using different excitation wavelengths. The key observations of the study are as follows:

- Increasing dilution delays the inception of PAH by over 2.5 ms as the intake-O_2 mole-fraction decreases from 15.0% to 9.0%.
- Though ignition and combustion do indeed occur at 7.5% intake-O_2 mole-fraction condition and with 800-bar CR fuel-pressure, neither soot nor large PAH are observed.
- At 9.0% intake-O_2, large PAH appears broadly in the jet-jet interaction regions, without any soot.
- At the dilution-threshold of soot formation, increasing intake-O_2 mole-fraction from 9.0% to 10.0% leads to soot formation in thin ribbons near the periphery of a PAH region that is broadly distributed throughout the cross-section of the downstream jets and along the bowl-wall.

The first appearance of soot at higher intake-O_2 mole-fractions than PAH is consistent with a lower temperature threshold for PAH than for soot formation.

- The spatial distributions of PAH and soot overlap slightly under these threshold-sooting conditions, with soot typically surrounding the PAH. The minimal overlap also suggests that PAHs are rapidly consumed and/or adsorbed when soot is formed.
- With increasing intake-O_2, the delay time between soot and PAH shortens, and soot tends to shift upstream to the jet region prior to wall impingement, though still on the periphery of the PAH.
- As the CR fuel-pressure is increased from 533 to 800 to 1200 bar at 9.0% intake-O_2, large PAH first forms at 800 bar, while soot first appears at 1200 bar. The spatial distribution of soot is consistent with observations at the dilution threshold, with soot formation at the fuel-pressure threshold also occurring at the PAH periphery. This may be explained by increased local temperatures at the higher mixing rates driven by the higher injection pressure. Additionally, this increasing soot trend is contrary to the decreasing soot trend with increasing fuel-pressure observed for conventional quasi-steady diesel jets.
- Initial formation of larger PAH occurs later and farther downstream than smaller PAH, shifting more into the jet-jet interaction regions rather than near the nominal jet axis.

References

1. Johnson T, “Diesel engine emissions and their control,” *Platinum Metals Review.* 50(1):23-37, 2008, doi:10.1595/147106708X248750
2. "Review of the research program of the U.S. DRIVE Partnership: Fifth Report." Washington, DC: The National Academies Press, 3-5, 2017, doi:10.17226/24717.
3. Dempsey A, Curran S, Wanger R, “A perspective on the range of gasoline compression ignition combustion strategies for high engine efficiency and low NOx and soot emissions: effects of in-cylinder fuel stratification,” *Int. J. Engine Res.* 17(8):897-917, 2016, doi:10.1177/1468087415621805.
4. Ravindar K, Sohki R, Grieken RV, "Atmospheric polycyclic aromatic hydrocarbons: source attribution, emission factors and regulation," *Atmos. Environ.*, 42(2008):2895-2921, 2008, doi:10.1016/j.atmosenv.2007.12.010.
5. Johansson O, Head-Gordon M, Schrader P et al., “Resonance-stabilized hydrocarbon-radical chain reactions may explain soot inception and growth,” *Science* 361:997-1000, 2018, doi:10.1126/science.aat3417.
6. Liu B, Xue Z, Zhu X, et al., "Long-term trends (1990-2014), health risks, and sources of atmospheric polycyclic aromatic hydrocarbons (PAHs) in the U.S.," *Environ Pollut.* 220:1171-1179, 2017, doi:10.1016/j.envpol.2016.11.018.
7. Bengtsson P, Aldén M, “Soot-visualization strategies using laser techniques,” *Applied Physics B*. 60(1):51-59, 1995, doi:10.1007/BF01082073.
8. Wal V, “Investigation of soot precursor carbonization using laser-induced fluorescence and laser-induced incandescence,” *Combust. Flame.* 110(1-2):281-284, 1997, doi:10.1016/S0001-20180(97)00072-2.
9. Wal V, “Soot precursor carbonization: Visualization using LIF and LII and comparison using bright and dark field TEM,” *Combust. Flame.* 112(4):607-616, 1998, doi:10.1016/S0010-20180(97)00171-5.
10. McCrain L, Roberts W, “Measurements of the soot volume field in laminar diffusion flames at elevated pressures,” *Combust. Flame.* 140(1-2):60-69, 2005, doi:10.1016/j.combustflame.2004.10.005.
11. Yoon S, Lee S, Chung S, “Effect of mixing methane, ethane, propane, and propene on the synergistic effect of PAH and soot formation in ethylene-based counterflow diffusion flames,” *Proc. Combust. Inst.* 30(1):1417-1424, 2005, doi:10.1016/j.proci.2004.08.038
12. Lee S, Turns S, Santoro R, “Measurements of soot, OH, and PAH concentrations in turbulent ethylene/air jet flames,” *Combust. Flame.* 156(12):2264-2275, 2009, doi:10.1016/j.combustflame.2009.09.005.
13. Choi B, Choi S, Chung S, “Soot formation characteristics of gasoline surrogate fuels in counterflow diffusion flames,” *Proc. Combust. Inst.* 33(1):609-616, 2011, doi:10.1016/j.proci.2010.06.067.
14. Oliveira, M., Olofsson, N., Johnsson, J., et al., “Soot, PAH and OH measurements in vaporized liquid fuel flames,” *Fuel.* 112:145-152, 2013, doi:10.11016/j.fuel.2013.05.006
15. Lemaire, R., Faccinetto, A., Therssen, E., et al., “Experimental comparison of soot formation in turbulent flames of Diesel and surrogate Diesel fuels,” *Proc. of Combust. Institute.* 32(1):737-744, 2009, doi:10.1016/j.proci.2008.05.019.
16. Zhou, L., Xiong, G., Zhang, M., et al., “Experimental study of polycyclic aromatic hydrocarbons (PAHs) in n-heptane laminar diffusion flames from 1.0 to 3.0 bar,” *Fuel* 209:265-273, 2017, doi:10.1016/j.fuel.2017.07.074.
17. Leermakers CJ, Musculus MPB, “In-cylinder soot precursor growth in a low-temperature combustion diesel engine: Laser-induced fluorescence of polycyclic aromatic hydrocarbons,” *Proc. Combust. Institute.* 35(3):3079-3086, 2015, doi:10.1016/j.proci.2014.06.101.
18. Bobba M, Musculus MPB, “Laser diagnostics of soot precursors in a heavy-duty diesel engine at low-temperature combustion conditions,” *Combust. Flame.* 159(2):832-843, 2012, doi:10.1016/j.combustflame.2011.07.017.
19. Genzale C, Reitz R, Musculus M, “Optical diagnostics and multi-dimensional modeling of spray targeting effects in late-injection low-temperature diesel combustion,” *SAE Int. J. Engines* 2(2):150-172, 2010, doi:10.4271/2009-01-2699.
20. O'Connor J, Musculus MPB, "In-cylinder mechanisms of soot reduction by close-coupled post-injections as revealed by imaging of soot luminosity and planar laser-induced soot incandescence in a heavy-duty diesel engine," *SAE Int. J. Engines* 7(2):673-693, 2014, doi:10.4271/2014-01-1255.
21. Espey C, Dec J, “Diesel engine combustion studies in a newly designed optical-access engine using high-speed visualization and 2-D laser imaging,” SAE Technical Paper 930971, 1993, doi:10.4271/930971.
22. Dec J, “A conceptual model of DI diesel combustion based on laser-sheet imaging,” SAE Technical Paper 970873, 1997, doi:10.4271/970873.
23. Murphy J, Taylor D, McCormick L, “Compendium of experimental cetane number data,” National Renewable Energy Laboratory NREL/SR- 540-36805, 2004.
24. Bacha J, Freel J, Gibbs A, et al.,“Diesel fuels technical review” Chevron Document MS-9915 (06-07), 2007.
25. Idicheria C, Pickett L, “Ignition, soot formation, and end of combustion transients in diesel combustion under high-EGR conditions,” *Int. J. Engine Res*. 12(4):376-392, 2011.

26. Eckbreth AC, *Laser diagnostics for combustion temperature and species*, Vol. 3. CRC Press, 1996
27. Musculus M, Lachaux T, Pickett L, et al., "End-of-injection over-mixing and unburned hydrocarbon emissions in low-temperature-combustion diesel engines," SAE Technical Paper 2007-01-0907, 2007, doi:10.4271/2007-01-0907.
28. Viteri F, Salinas J, Millera A, et al., "Pyrolysis of dimethyl carbonate: PAH formation," *J. Anal. Appl. Pyrolysis.* 122:524-530, 2016, doi:10.1016/j.jaap.2016.09.011.
29. Pickett L, Siebers D, Idicheria C, "Relationship between ignition processes and the lift-off length of diesel fuel jets," SAE Technical Paper 2005-01-3843, 2005, doi:10.4271/2005-01-3843.
30. Pickett L, Caton J, Musculus M, et al., "Evaluation of the equivalence ratio-temperature region of diesel soot precursor formation using a two-stage Lagrangian model," *Int. J. Engine Res.* 7(5):349-370, 2006, doi:10.1243/14680874JER00606.
31. Wang H, Qi J, Yao M, et al., "Development of an n-heptane/toluene/Polyaromatic hydrocarbon mechanism and its application for combustion and soot prediction," *Int. J. Engine Res.* 14(5):434-451, 2013, doi:10.1177/1468087412471056.
32. Skeen S, Yasutomi K, "Measuring the soot onset temperature in high-pressure n-dodecane spray pyrolysis," Combust. Flame. 188: 483-487, 2018, doi:10.1016/j.combustflame.2017.09.030.
33. Aronsson U, Chartier C, Andersson Ö, et al., "Analysis of correlation between engine-out particulates and local ϕ in the lift-off region of a heavy duty diesel engine using Raman spectroscopy," *SAE Int. J. Fuels Lubr.* 2(1):645-660, doi:10.4271/2009-01-1357.
34. Hildingsson L, Persson H, Johansson B, et al., "Optical diagnostics of HCCI and low-temperature diesel using simultaneous 2-D PLIF of OH and formaldehyde," SAE Technical Paper 2004-01-2949, 2004, doi:10.4271/2004-01-2949.
35. Genzale C, Reitz R, Musculus M, "Effects of piston bowl geometry on mixture development and late-injection low-temperature combustion in a heavy-duty diesel engine," *SAE Int. J. Engines* 1(1):913-937, 2009, doi:10.4271/2008-01-1330.

Contact Information

Zheming Li, zheli@sandia.gov

Acknowledgments

This research was sponsored by the U.S. Department of Energy (DOE) Office of Energy Efficiency and Renewable Energy (EERE), with program managers Michael Weismiller and Gurpreet Singh. Experiments were conducted at the Combustion Research Facility, Sandia National Laboratories, Livermore, CA. Sandia National Laboratories is a multi-mission laboratory managed and operated by National Technology and Engineering Solutions of Sandia, LLC., a wholly owned subsidiary of Honeywell International, Inc., for the U.S. Department of Energy's National Nuclear Security Administration under contract DE-NA0003525.

The authors thank Dave Cicone, Keith Penney, and Gary Hubbard for their dedicated support of the Sandia/Cummins heavy-duty optical engine. The authors highly appreciate the fruitful discussion with Lyle Pickett and Scott Skeen regarding the CR fuel-pressure effects on soot and PAH formation.

Definitions/Abbreviations

AHRR	apparent heat release rate
ºCA	degrees crank angle
CAD	crank angle degree
CR	common rail
DSE	duration of solenoid energizing
ECN	engine combustion network
EGR	exhaust-gas recirculation
ICCD	intensified charge-coupled device
IMEPg	gross indicated mean effective pressure
LTC	low-temperature combustion
LWP	long wave-pass
NO_x	nitrogen oxides
OPO	optical parameter oscillator
PAH	polycyclic aromatic hydrocarbons
PLIF	planar laser induced fluorescence
PLII	planar laser induced incandescence
S/N	Signal-to-noise ratio
SSE	start of solenoid energizing
SWP	short wave-pass
TDC	top dead center
TSL	two-stage Lagrangian
UV	ultraviolet
ϕ	equivalence ratio (phi)

Appendix

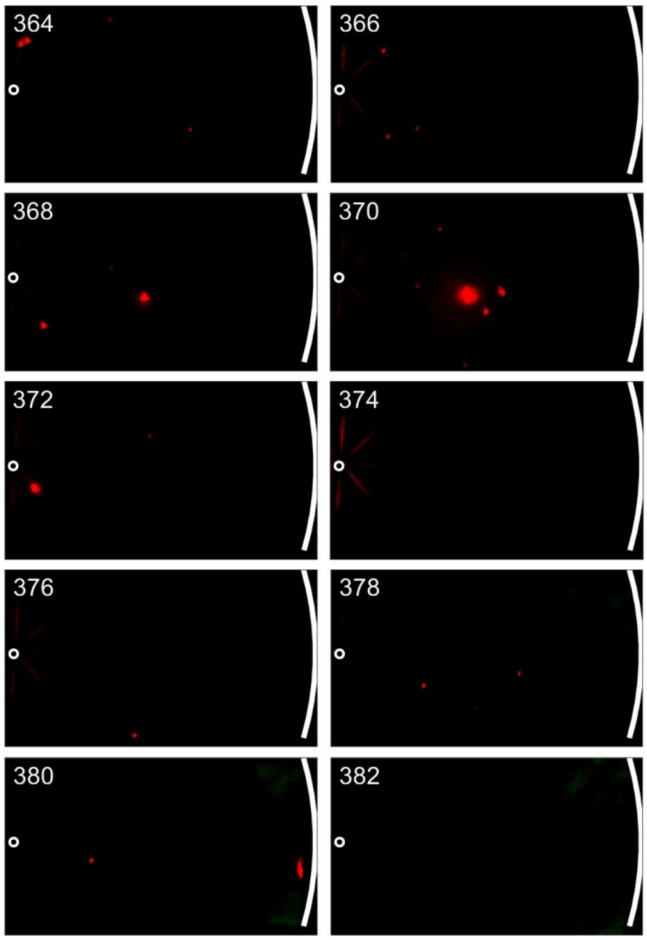

Figure A1. Composite images of ensemble-averaged 633-nm PAH-PLIF (false-colored green) and soot-PLII (red) with 9.0% intake-O_2 and 533-bar CR fuel-pressure. The CAD of image acquisition is shown in the upper left corner of each image.

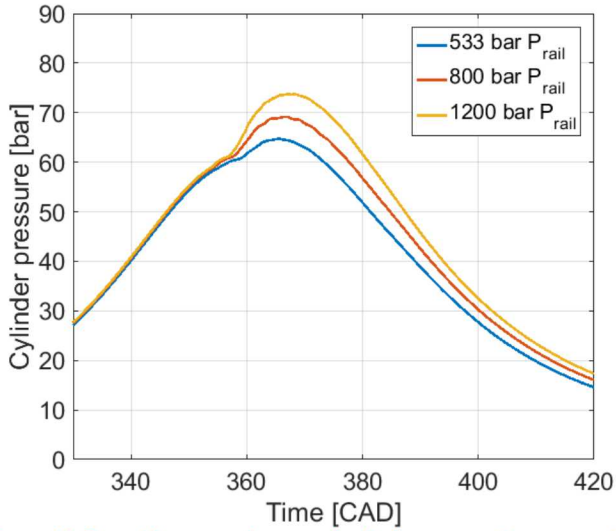

Figure A2. Ensemble-averaged measured cylinder-pressure for a sweep of CR fuel-pressure at 9.0% intake-O_2 mole-fraction (see Table 3 for operating conditions).